RESEARCH: Original Research

ELSEVIER

Chemical short-range order in multi-principal element alloy with ordering effects on water electrolysis performance

Yiyuan Yang [a], Zhe Jia [a,*], Xinyue Zhang [a], Yujing Liu [b], Qianqian Wang [a], Yongjie Li [a], Liliang Shao [a], Siyi Di [a], Juan Kuang [a], Ligang Sun [c,*], Lai-Chang Zhang [d], Jamie J. Kruzic [e], Yang Lu [f,*], Jian Lu [g], Baolong Shen [a,*]

[a] School of Materials Science and Engineering, Jiangsu Key Laboratory for Advanced Metallic Materials, Southeast University, Nanjing 211189, China
[b] Institute of Metals, College of Materials Science and Engineering, Changsha University of Science & Technology, Changsha 410114, China
[c] School of Science, Harbin Institute of Technology, Shenzhen 518055, China
[d] Centre for Advanced Materials and Manufacturing, School of Engineering, Edith Cowan University, 270 Joondalup Drive, Joondalup, Perth, WA 6027, Australia
[e] School of Mechanical and Manufacturing Engineering, University of New South Wales (UNSW Sydney), Sydney, NSW 2052, Australia
[f] Department of Mechanical Engineering, The University of Hong Kong, Pokfulam Road, Hong Kong Special Administrative Region
[g] Hong Kong Branch of National Precious Metals Material Engineering Research Center and Department of Mechanical Engineering, City University of Hong Kong, Hong Kong Special Administrative Region

The superior electrocatalytic activity of multi-principal element alloys (MPEAs) is typically attributed to synergistic effects of their multi components in random solid solutions. Strategies to control the functional atoms with a chemically ordered atomic distribution and the specific atomic configuration in the MPEAs remain a challenging research topic. Here, we have discovered non-random, chemical short-range order (CSRO) in a $Fe_{10}Co_5Ni_{10}Cu_{15}Al_{60}$ MPEA induced by magnetic characteristics of elements, leading to ultralow overpotential for dual-electrode water splitting in alkaline condition. Atomic-resolution imaging and elemental mapping assisted by statistical analysis and density functional theory (DFT) simulations revealed that CSRO in the MPEA originated from the nearest-neighbor preference of M-Cu (M = Fe, Co, Ni, and Al) pairs and repulsion of same-element pairs (Fe-Fe, Co-Co, Ni-Ni, Cu-Cu, and Al-Al). Such preferential atomic pairs facilitated H_2O/H^* adsorption/desorption during the hydrogen evolution reaction and reduced the energy barrier for the rate-determining step of the oxygen evolution reaction, thereby promoting excellent overall water splitting performance. The achieved current density (130 mA cm^{-2}) of the low-cost MPEA was ~4 times higher than that of the Pt/C||RuO$_2$ dual-electrode system (32 mA cm^{-2}) at a cell voltage of 2.0 V. The concept of CSRO in MPEAs offers new insights into their multi-functional applications, potentially spurring the development of numerous high-performance MPEA-based devices for the energy and environmental sectors.

Keywords: Chemical short-range order; Multi-principal element alloy; Metallurgy; Atomic configuration; Water splitting

* Corresponding authors.
   E-mail addresses: Jia, Z. (zhejia@seu.edu.cn), Sun, L. (sunligang@hit.edu.cn), Lu, Y. (ylu1@hku.hk), Shen, B. (blshen@seu.edu.cn).

Introduction

Hydrogen is widely considered as a clean and sustainable energy source to replace traditional fossil fuels and help the world transition to a carbon–neutral society [1]. For hydrogen production, electrochemical water splitting is an appealing and promising alternative to steam reforming due to its simplicity and zero carbon emissions [2–6]. However, the lack of high-performance and low-cost electrocatalysts greatly limits the rapid development of this technology. To address these requirements, multi-principal element alloys (MPEAs) [7,8], generally including medium-entropy alloys (MEAs) and high-entropy alloys (HEAs) have recently received extensive interests for the discovery of new electrocatalysts due to their unique physicochemical characteristics [9–16], and promising candidates have been reported including high-entropy intermetallics (HEIs) [17,18], high-entropy metallic glasses (HEMGs) [19–22] as well as high-entropy oxides/hydroxides [23,24], nitrides [25], phosphides [26], sulfides [27], metal–organic frameworks [28]. However, existing research on MPEAs is mostly focused on the development of underexplored compositional space and randomly disordered chemical distribution in a solid-solution phase. Strategies to control the functional atoms with a chemically ordered atomic distribution and the specific atomic configuration in the MPEAs would best promote the electrochemical reaction.

Chemical short-range order (CSRO), which is typically induced by enthalpic interactions among constituent atoms and is directly correlated to chemically preferred atomic pairs [29], has been recently observed in MPEAs such as VCoNi [30], CrCoNi [31], TiZrHfNb [32,33], MoTaTiWZr [34], and FeCoNiCrCuAl [35]. Studies show that CSRO might originate from multi-factors, such as local strain energy caused by atomic size differences [35,36], mixing enthalpy between various principal elements [37], electronic states regulation [38], and resulting magnetic interactions between the constituent elements [39]. The theoretical basis for the formation of CSRO in MPEAs, and its effect on the material properties, are ongoing areas of research. It is becoming widely accepted that CSRO is inclined to form in MPEAs at specific temperature, and in some cases, it may have great potential to influence the local atomic configurations and the macroscopic properties of MPEAs [30,40,41]. However, the characterization and modeling of CSRO in complex solid solutions remains a challenging research topic, and to date the effect of CSRO on electrocatalytic performance is far from being understood.

In this study, to uncover the potential benefits of CSRO on the electrocatalytic performance of MPEAs, we have developed a porous $Fe_{10}Co_5Ni_{10}Cu_{15}Al_{60}$ MPEA that possesses large amounts of active sites constructed by M-Cu (M = Fe, Co, Ni, Al) atomic pairs to achieve outstanding water electrolysis activity in alkaline condition. The preferential atomic occupancy of neighboring lattice planes in the CSRO was systematically characterized by atomic-resolution mapping, statistical analysis, and selected area electron diffraction (SAED) to confirm the existence of the nearest neighbor preference of M-Cu (M = Fe, Co, Ni, Al) as well as the repulsion of the same elemental pairs (Fe-Fe, Co-Co, Ni-Ni, Cu-Cu, and Al-Al). Density functional theory (DFT) simulations revealed that the preferred M-Cu atomic pairs exhibited a much lower energy barrier for hydrogen evolution reaction (HER) than the randomly disordered atomic configuration, and the oxygen evolution reaction (OER) performance was enhanced owing to the favorable thermodynamics of the generated metal hydroxides and weakened interaction between the Cu sites and O* species in the CSRO regions.

Materials and methods

Materials

Fe (99.99 wt%), Co (99.99 wt%), Ni (99.99 wt%), Cu (99.99 wt %), and Al (99.99 wt%) granules were weighed and mixed to give a theoretical atomic composition of $Fe_{10}Co_5Ni_{10}Cu_{15}Al_{60}$. Analytical grade potassium hydroxide (KOH) and absolute ethanol were supplied by Aladdin (Shanghai, China) and Nanjing WANQING Chemical Glassware & Instrument Co., Ltd (Nanjing, China). Deionized water was used to dilute the KOH solutions. IrO_2 and RuO_2 were supplied by Macklin (Shanghai, China), and 20 % Pt/C was supplied by Johnson Matthey (London, England).

Materials preparation

The MPEA ribbons were prepared by arc-melting and melt-spinning methods. Specifically, a master alloy ingot (∼20 g) with an atomic composition of $Fe_{10}Co_5Ni_{10}Cu_{15}Al_{60}$ was initially prepared by arc-melting under high-purity argon (Ar) atmosphere with Ti-gettering to minimize oxidation. The ingot was remelted at least four times to ensure the homogeneity of metal elements. Afterwards, the master alloy ingot was cut into pieces that were remelted in a quartz crucible and then ejected onto a rotating Cu wheel surface (10 m s^{-1}). The whole process was under Ar atmosphere. The as-spun MPEA ribbons were cut into 0.3 × 1 c m^2 segments as freestanding electrodes that were used throughout this work. With regard to the chemical dealloying process, the as-spun MPEA ribbons were treated in a 3.0 M KOH solution at different time intervals of 2, 4, 6, and 9 h. The dealloyed MPEA ribbons were then washed by deionized water and ethanol three times.

Materials characterization

X-ray diffraction (XRD) experiments were performed using a Bruker D8-Discover diffractometer with Cu-Kα radiation with a step size of 0.02° and a scan rate of 0.15 s per step. Surface morphology was investigated using a scanning electron microscope (SEM, Nova Nano SEM450). Microstructure was analyzed employing a high-resolution transmission electron microscope (HRTEM, Talos F200X) coupled with SAED and energy-dispersive spectrometry (EDS). The used specimens were prepared using ion beam milling (Gatan-691) technique from one side to the other. This method ensured the resulting sample piece was the surface of the MPEA ribbon. Atomic-resolution scanning transmission electron microscopy (STEM) images and EDS mappings were acquired using a double spherical aberration corrected transmission electron microscope (AC-TEM, FEI-Themis Z). The AC-TEM specimen was prepared using an FEI focused ion beam/scanning electron microscope (FIB/SEM). X-ray photoelectron spectroscopy (XPS) spectra were collected using a Thermo Scientific K-Alpha instrument. The leached metallic ions after stability

experiments were quantified by inductively coupled plasma-optical emission spectrometry (ICP-OES).

Statistical analysis

Forty line-scan profiles were collected to ensure the accuracy of the statistical analysis. The analysis was conducted with the help of Matlab. Firstly, a spline representation of the discrete atomic concentration points covered in the EDS line scan profiles was required to be interpolated to calculate the derivatives at any location (r). Then, the location of each A-enriched (A = Fe, Co, Ni, Cu, Al) column were identified in the forty EDS line profiles following three criteria:

(i) $\chi'_A(r) = 0$, for locating the A-enriched/A-depleted column positions;
(ii) $\chi''_A(r) < 0$, for locating the A-enriched column positions;
(iii) $\chi_A(r) > \bar{\chi}_A(r)$, where the $\chi_A(r)$ represents the concentration of A, and $\chi'_A(r)$, $\chi''_A(r)$, and $\bar{\chi}_A(r)$ are the 1st derivative, 2nd derivative, and average of A in the EDS line profiles, respectively.

After locating the explicit positions of the atomic columns, the distance distributions between the A- and B-enriched columns were determined, where the A-B pair could be any two out of the Fe, Co, Ni, Cu, and Al. The frequency distribution histograms of the distance between two atomic columns were plotted with three representative bin widths of 0.01, 0.015, and 0.02 nm.

Electrochemical measurements

The electrocatalytic performance was conducted using a standard three-electrode electrochemical station (Gamry Interface 1000) in a 1.0 M KOH solution. Graphite rod, Hg/HgO electrode, and the MPEA ribbon were used as the counter electrode, reference electrode, and the freestanding working electrode, respectively. The performance of commercial IrO_2, RuO_2, and Pt/C catalysts were investigated for activity comparison. The IrO_2, RuO_2, and Pt/C inks were loaded on a glass carbon electrode (0.07 cm^2) with mass loading of 0.43 mg cm^{-2} (IrO_2, RuO_2) and 0.17 mg cm^{-2} (Pt/C), respectively. The current density was calculated from the measured geometric surface area. All potentials reported in this work were calibrated against reversible hydrogen electrode (RHE) with the following equation: $E_{RHE} = E_{Hg/HgO} + 0.0591 \times$ pH + 0.098. All samples underwent cyclic voltammetry (CV) with 50 cycles at a scan rate of 100 mV s^{-1} to reach a steady state before electrochemical measurements. Linear sweep voltammetry (LSV) for HER and OER were carried out with a scan rate of 5 mV s^{-1} by iR compensation. Electrochemical impedance spectroscopy (EIS) was carried out from 0.1 to 10^5 Hz. Double-layer capacitance (C_{dl}) was determined by measuring a series of CVs at sweep rates from 10 to 50 mV s^{-1} in the non-faradaic potential region. The electrochemical surface areas (ECSAs) were calculated according to the equation of ECSA = C_{dl}/C_s, where C_s is the specific capacitance per unit area. In this work, C_s was chosen as 0.04 mF cm^{-2} in 1.0 M KOH. Chronoamperometry tests at static current densities of 20 and 50 mA cm^{-2} without iR loss correction were used to evaluate the stability of the catalysts. With respect to the cost estimation, we calculated the cost of raw materials per kilogram of various electrocatalysts based on the atomic composition for comparison. The cost per kilogram of raw materials based on the mole ratio of each component for various electrocatalysts was calculated through the following criterion: $Cost = \sum_i^n p_i \times \alpha_i$, where n is the total number of principal elements, p_i is the cost (unit: USD/kg) of each element i, α_i is the atomic ratio (at.%) of each element i. The price of various raw metals is obtained from ZhongNuo Advanced Material (Beijing) Technology Co., Ltd.

DFT simulations

Spin-polarized DFT calculations were conducted to provide the atomic mechanisms responsible for the overall water splitting behavior of the $Fe_{10}Co_5Ni_{10}Cu_{15}Al_{60}$ MPEAs using the Cambridge Sequential Total Energy Package (CASTEP) module in Materials Studio software. The generalized gradient approximation method with the Perdew-Burke-Ernzerh function (GGA-PBE) was employed to describe the exchange and corrections of atomic interaction. The interactions between valence electrons and ionic cores were calculated using the ultrasoft pseudopotential method. A plane-wave basis set with a cutoff energy of 400 eV was assigned. The Brillouin zone was sampled by a Monkhorst-Pack grid [42]. The tolerances of energy, force, and displacement for structure optimization were 10^{-5} eV/atom, 0.03 eV/Å, and 0.002 Å respectively. The self-consistence field (SCF) was set as 5×10^{-6} eV/atom.

The H_2O adsorption energies (ΔE_{H_2O}) at the surface of the catalysts were calculated by the equation:

$$\Delta E_{H_2O} = E_{surf+H_2O} - E_{surf} - E_{H_2O} \tag{1}$$

where the E_{surf} and E_{surf+H_2O} are the total energies of the catalyst surface before and after water adsorption, and E_{H_2O} is the energy of a free water molecule.

The Gibbs free energies for hydrogen adsorption (ΔG_{H*}) were calculated from the equation:

$$\Delta G_{H*} = \Delta E_{H*} + \Delta ZPE - T\Delta S \tag{2}$$

where the ΔE_{H*}, ΔZPE, T, and ΔS represent the binding energy, zero-point energy change, temperature, and entropy change of the H adsorption system, respectively.

The vibrational entropy of H at the adsorbed state is assumed to be negligible. Thus, ΔS can be obtained from the following equation:

$$\Delta S = S_{H*} - \frac{1}{2}S_{H_2} \approx -\frac{1}{2}S_{H_2} \tag{3}$$

where S_{H_2} is the entropy of H_2 in the gas phase under standard conditions.

ΔZPE can be calculated from the equation:

$$\Delta ZPE = ZPE_{H*} - \frac{1}{2}ZPE_{H_2} \tag{4}$$

and ΔG_{H*} can be calculated using the simplified equation [43]:

$$\Delta G_{H*} = \Delta E_{H*} + 0.24 \text{ eV} \tag{5}$$

The OER investigation was performed using previously reported procedures [44]. The reaction free energy for adsorbate during the OER process was obtained by structure optimization

of intermediates. The OER proceeds in four electron steps which can be analyzed by calculating the reaction free energies of all basic steps along the reaction coordinates:

(1) Dissociation of hydroxide ions into OH* followed by surface adsorption;
(2) Formation of O* and H_2O by the reaction between OH* and OH^-;
(3) Reaction between O* and hydroxide ions to form OOH*;
(4) Reaction between OOH* and hydroxide ions to produce O_2.

Five representative atomistic models, with highly similar composition and structure obtained in our experiments, were constructed to investigate their contribution to the overall water splitting performance: (a) FeOOH with (211) surface (named as "FeOOH-211"); (b) FeOOH with (321) surface (named as "FeOOH-321"); (c) CoOOH with (020) surface (named as "CoOOH-020") (d) face-centered cubic $Fe_{10}Co_5Ni_{10}Cu_{15}Al_{60}$ with randomly distributed atomic composition (named as "MPEA-Random"); (e) body-centered cubic $Fe_{10}Co_5Ni_{10}Cu_{15}Al_{60}$ with chemical short-range ordered atomic composition (named

as "MPEA-CSRO"). Structural optimizations were performed for those models to optimize the crystal structures, setting different k points that were appropriate for the respective models. Then, the (211) and (321) surfaces for FeOOH, the (020) surface for CoOOH, and the (111) surface for the MPEA-Random and MPEA-CSRO models were cleaved from the optimized periodic structures with a vacuum layer of ~15 Å. These surface models were further geometrically optimized and used to study the overall water splitting performance of the $Fe_{10}Co_5Ni_{10}Cu_{15}Al_{60}$ MPEA, especially focusing on investigating the potential effect of chemical short-range order.

Results

Alloy design and preparation

The MPEAs design was based on the energy minimum principle associated with local atomic moments of elements, which we predicted atomic-scale ordering driven by magnetic interactions between the constituents [29,39,40,45]. Five principal components with different magnetic properties were selected: ferromagnetism of Fe, Co, and Ni, paramagnetism of Al, and diamagnetism of Cu. It was predicted that repulsion between
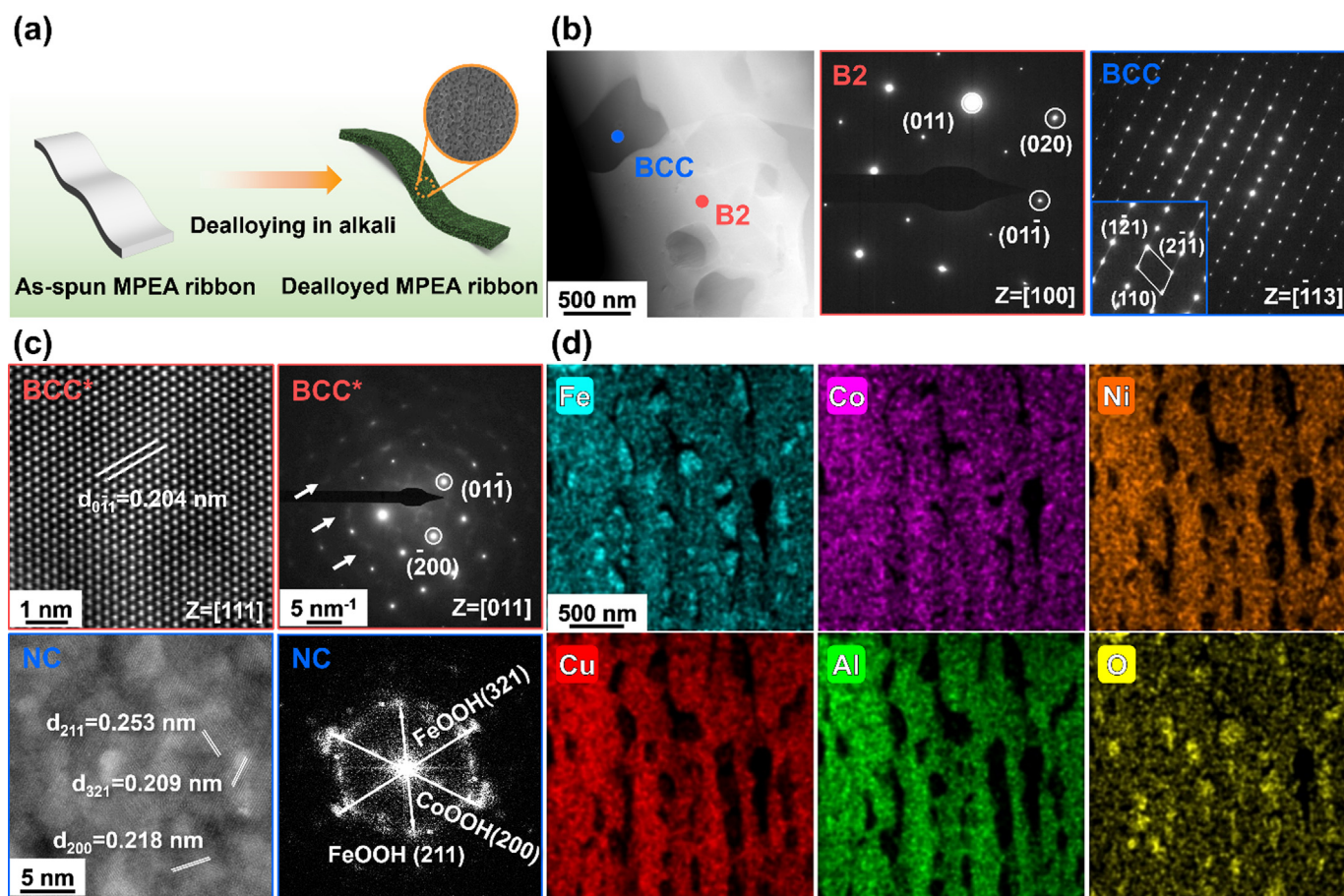

FIG. 1

Conceptual design and microstructural characterization of the MPEA. (**a**) Schematic of the preparation process. (**b**) TEM image with the corresponding SAED patterns of the B2 and BCC phases corresponding to the as-spun MPEA ribbon. The inset shows a magnified view of the SAED pattern for the BCC phase. (**c**) AC-TEM images and SAED patterns showing the evolution of the B2 phase into a chemically short-range ordered BCC* phase and the evolution of the BCC phase into a nanocrystalline structure for the D4h MPEA ribbon, respectively. (**d**) Cross-sectional EDS mapping results for the D4h MPEA ribbon.

Cu-Cu pairs [39,45] resulted in the formation of specific preferential nearest neighbors of Cu-M (M = Fe, Co, Ni, Al). Accordingly, the melt-spun MPEA ribbon with an atomic composition of Fe_{10}-$Co_5Ni_{10}Cu_{15}Al_{60}$ was prepared by a physical metallurgical technique [46]. Fig. 1a schematically illustrates the surface morphology evolution in a 3.0 M KOH solution at room temperature (298 K), in which the as-spun MPEA ribbons were used as precursors to produce the self-supported electrodes used in this work. SEM images indicated that the as-spun MPEA had a smooth surface (Supplementary Fig. 1a). The XRD results indicated that the as-spun MPEA possessed a dual-phase structure consisting of a body-centered cubic (BCC) phase and a B2 phase (Supplementary Fig. 2a). The diffraction peaks of BCC and B2 phases overlapped at 44.5°, 64.5°, and 81.6°, and the peak at 31.1° distinctly represented the B2 phase [47]. To further confirm the dual-phase structure of the as-spun MPEA, TEM characterization is shown in Fig. 1b, where the B2 (red dot) and BCC (blue dot) phases were clearly distinguished based on different contrast. The SAED pattern of the B2 phase presented superlattice spots [48] (Fig. 1b), and the d-spacings of 0.203 nm and 0.201 nm were determined for their $\{0\,1\,1\}$ and $\{0\,1\,\bar{1}\}$ planes, respectively (Supplementary Fig. 3a). The BCC phase was also identified by the SAED pattern along the zone axis of $[\bar{1}\,1\,3]$ (Fig. 1b), and the measured lattice spacing of 1.155 nm for the $\{1\,\bar{2}\,1\}$ plane is shown in Supplementary Fig. 3b. The specific atomic compositions of the B2 and BCC phases were measured by EDS (Supplementary Table 1). The atomic contents of Al (67.7 %) and Fe (15.6 %) in the BCC phase were higher than in the B2 phase (Al: 46.7 % and Fe: 8.5 %), whereas the contents of Co, Ni, and Cu in the BCC phase (Co: 8.2 %, Ni: 4.6 %, and Cu: 3.9 %) were lower than in the B2 phase (Co: 4.5 %, Ni: 15.6 %, and Cu: 24.7 %). These results indicate that the as-spun MPEA ribbon contained dual-phase that are distinct both in crystalline structure and atomic composition.

Supplementary Fig. 1 shows surface morphology evolution towards porous architectures of the MPEA ribbon, where the ribbons dealloyed for various times of 2, 4, 6, and 9 h were denoted as D2h, D4h, D6h, and D9h, respectively. The D4h MPEA ribbon presented a homogeneous porous structure with an average pore size of 175 nm (Supplementary Fig. 1b), with a cross-sectional porous layer of 3.6 μm thick (Supplementary Fig. 4, indicating the specific surface area was improved which would be beneficial to the electrocatalytic performance. In terms of structural evolution, the peaks of the BCC phase gradually weakened with increasing dealloying time (Supplementary Fig. 2b), indicating that the BCC phase (with high content of Al) was relatively unstable in alkali. Fig. 1c shows the HRTEM images with corresponding SAED patterns of the D4h MPEA. It was found that the original BCC phase evolved into a nanocrystalline structure in the D4h MPEA (Fig. 1c, blue border, denoted as NC; Supplementary Fig. 5, blue dot) with interplanar spacings of 0.209, 0.253, and 0.218 nm, which corresponded to the indexed $\{3\,2\,1\}$ and $\{2\,1\,1\}$ planes for FeOOH and $\{2\,0\,0\}$ plane for CoOOH in the fast Fourier transform (FFT) pattern, respectively. Moreover, the superlattice spots of the original B2 phase in the as-spun MPEA (Fig. 1b, red border) were completely removed

after 4 h dealloying process (Fig. 1c, red border), which indicated that the original B2 phase had transformed into a traditional BCC structure (Supplementary Fig. 5, red dot; denoted as BCC* to distinguish it from the original BCC phase) with clear Bragg diffraction spots of $\{0\,1\,\bar{1}\}$ and $\{\bar{2}\,0\,0\}$ (white circles in Fig. 1c). We observed the presence of CSRO along the [0 1 1] axis of the BCC* phase (red border in Fig. 1c), wherein the weak square-like diffused scatterings between the transmission spot and $\{\bar{2}\,0\,0\}$ spots (white arrows) were attributable to the CSRO regions [30,31,49]. Fig. 1d and Supplementary Table 1 show the results of elemental analysis of the NC and BCC* phases in the D4h MPEA. Fe, Co, and O were relatively concentrated in the NC phase, whereas Fe, Co, Ni, Cu, and Al were homogeneously distributed in the BCC* phase. These findings indicated that the NC phase mostly consisted of the FeOOH and CoOOH species, and the BCC* phase was a solid solution phase. The evolution of chemical valence states on the MPEA surface at different dealloying time intervals was examined by XPS (Supplementary Fig. 6), and the discussion was shown in Supplementary Text 1.

Characterization of CSROs

To further confirm the detailed atomic configuration in the CSRO regions, AC-TEM and atomic-level EDS mapping analyses were conducted. Fig. 2a shows the AC high-angle annular dark field scanning TEM (HAADF-STEM) image of the BCC* phase. The corresponding FFT pattern (Fig. 2a inset) indicates diffuse scatterings (cyan circles) which could be assigned to the CSRO regions. High-resolution EDS mapping along the [111] zone axis of the BCC* phase is shown in Supplementary Fig. 7. Fig. 2b presents the atomic-level EDS mapping result for Fe and Cu. Each spot with a different color can be interpreted as an atomic column that is perpendicularly oriented along the thickness direction of the TEM sample. The brightness of the colored spots highly depends on the concentration of the particular atoms being probed. Four typical CSRO regions were selected, as shown in Fig. 2c, in which the occupancy of Fe and Cu atoms exhibited a certain regularity. Two Cu-enriched $(\bar{1}\,0\,1)$ planes (red dashed lines) sandwiched one Fe-enriched $(\bar{1}\,0\,1)$ plane (dashed cyan lines), that is, the Cu-enriched $(\bar{1}\,0\,1)$ planes were alternated with the planes that were enriched with Fe. Fig. 2d–i shows three groups of representative CSRO regions for Al-Cu, Co-Cu, and Ni-Cu atomic pairs, which presented similar CSRO characteristics with the Fe-Cu pair, that is, two Cu-enriched planes sandwiched one Cu-depleted (Al/Co/Ni-enriched) plane. Such chemical orderings are expected to double the interplanar spacing of the BCC* lattice, which is in good agreement with the observation of the diffraction spots at $\frac{1}{2}\{\bar{1}\,0\,1\}$ locations (Fig. 2a inset).

To quantify the observed CSRO in the BCC* phase, we performed a statistical analysis based on the EDS mapping results [30,31]. Forty line-scan profiles were collected along the $\{0\,\bar{1}\,1\}$ direction (white arrow in Fig. 2a) to ensure the accuracy of the statistical analysis. The red, cyan, pink, orange, and green curves in Fig. 3a indicate atomic fractions of Cu, Fe, Co, Ni, and
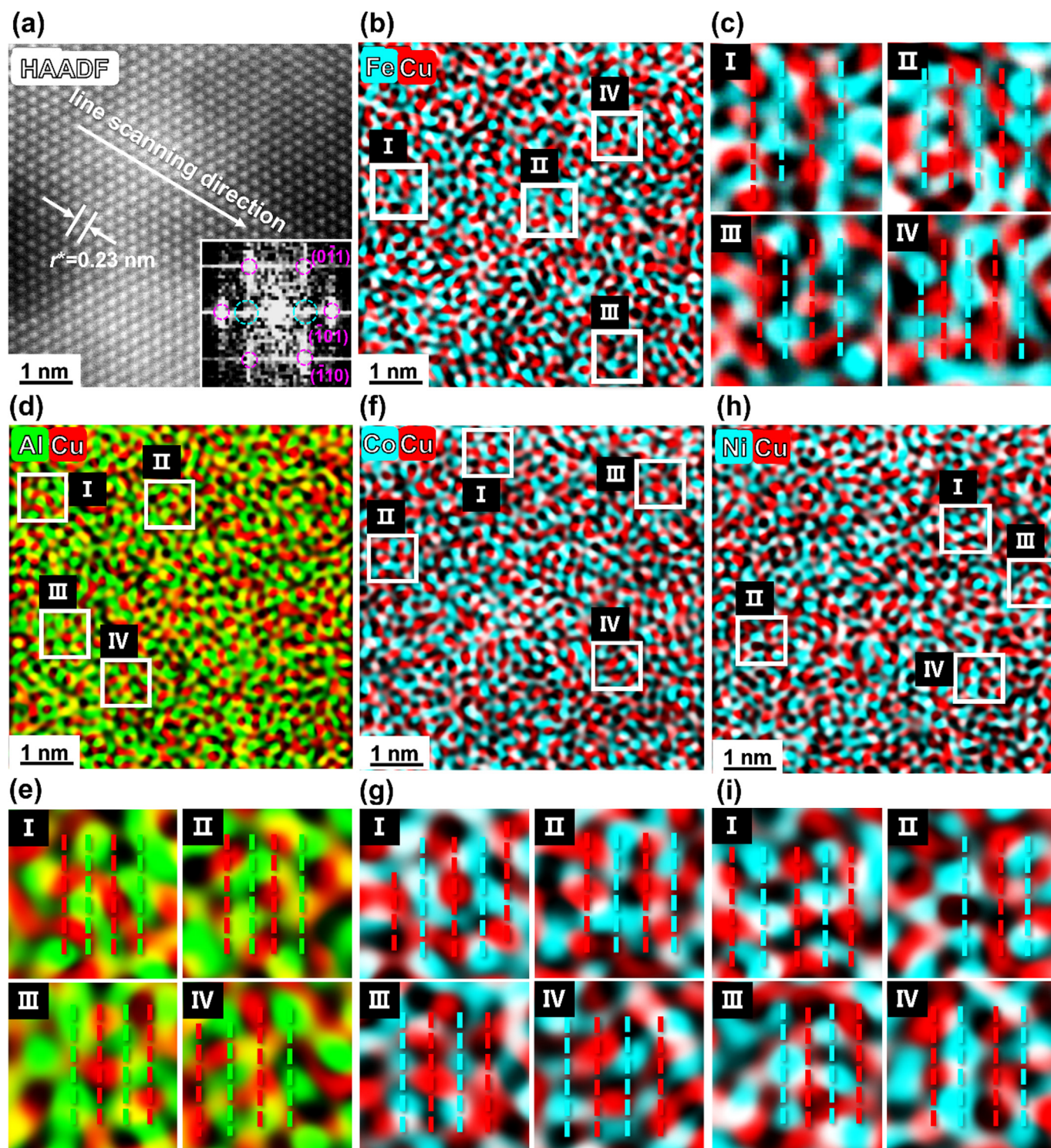
RESEARCH: Original Research

FIG. 2

Observation of CSRO regions and their atomic distribution in the BCC* phase. (**a**) HAADF-STEM image of the BCC* phase along the $[1\,1\,1]$ zone axis, inset is the FFT pattern showing extra diffraction spots at $\frac{1}{2}\left\{1\,0\,1\right\}$ (cyan circles), along with sharp Braggs spots from the BCC* phase (pink circles). The line-scanning direction and the value of the measured $r*$ are labeled in the image. EDS mapping results of (**b**) Fe-Cu, (**d**) Al-Cu, (**f**) Co-Cu, and (**h**) Ni-Cu atomic pairs, where the representative CSRO regions are marked by white boxes. Close-up maps of the representative CSRO regions of (**c**) Fe-Cu, (**e**) Al-Cu, (**g**) Co-Cu, and (**i**) Ni-Cu. The red dashed lines are the Cu-enriched planes. The cyan and green dashed lines are the Fe/Co/Ni and Al-enriched planes, respectively.

Al as a function of the distance, respectively. Firstly, a spline representation of the discrete atomic concentration points covered in the EDS line scan profiles was required to be interpolated to calculate the derivatives at any location (r). Then, we identified the location of each A-enriched (A = Fe, Co, Ni, Cu, Al) column in the forty EDS line profiles following three criteria: (i)
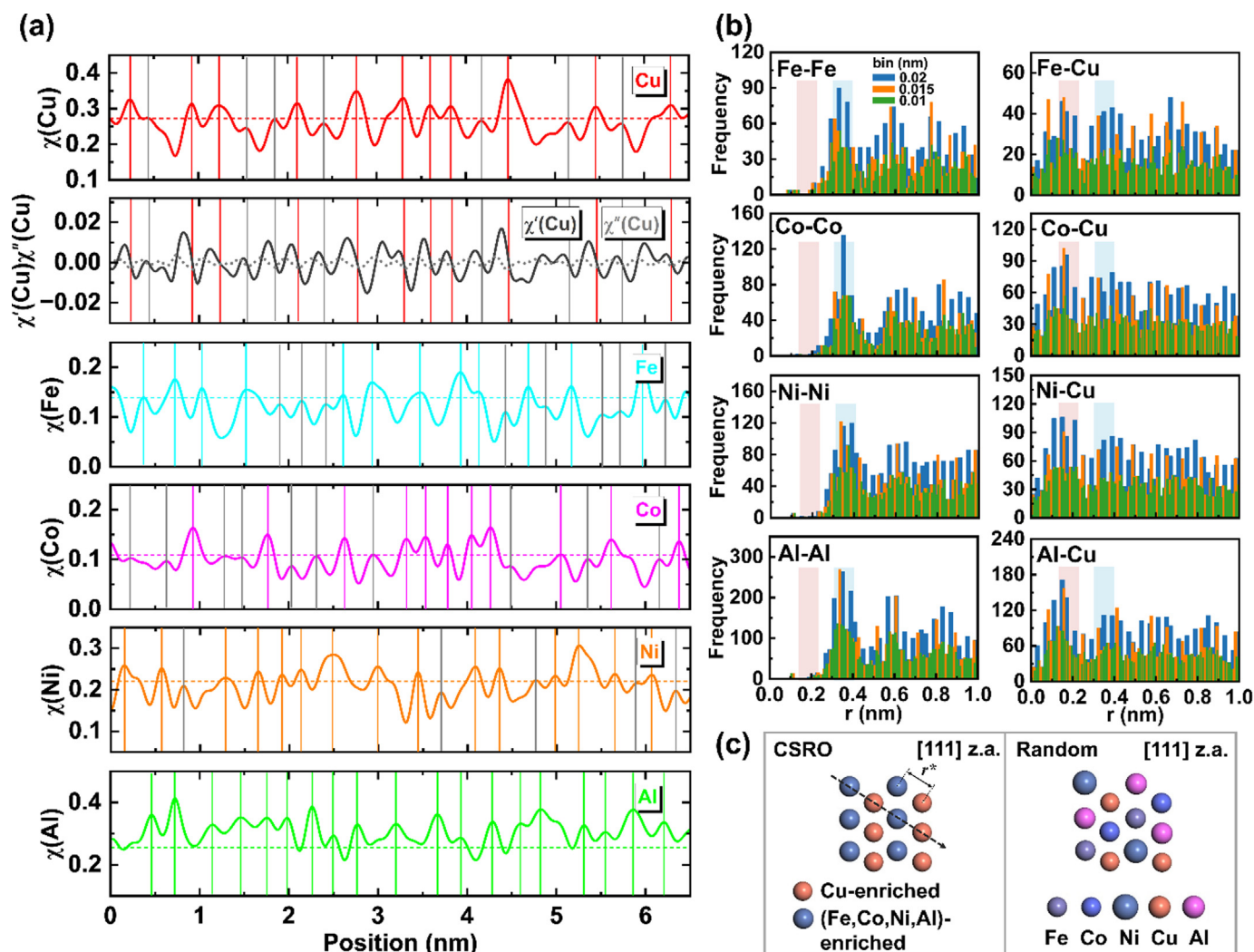
(a)

(b)

(c)

FIG. 3

Statistical analysis of CSRO in the BCC* phase based on energy-dispersive spectrometry line profiles. (**a**) Typical composition line profiles obtained from line scans in the $\boxed{0\ 1\ 1}$ direction. The red, cyan, pink, orange, and green vertical lines indicate the determined locations of Cu-, Fe-, Co-, Ni-, and Al-enriched columns. The 1st derivative, $\chi'_{Cu}(r)$ (dark grey solid line), and 2nd derivative, $\chi''_{Cu}(r)$ (light grey dotted line), are illustrated for the Cu concentration profile. The vertical grey lines are the local maxima with concentration lower than the sample average of each element (horizontal dotted line), which are excluded from the element-enriched columns. (**b**) Histogram plots show the frequency of A-B column pairs within three representative bin widths. A and B elements can be any two out of Fe, Co, Ni, Cu, and Al. (**c**) Schematics of CSRO and ideal random atomic arrangements along the $\boxed{1\ 1\ 1}$ zone axis. The dashed line shows the line scanning direction. The nearest neighbor atomic distance r^* is labeled in the picture.

$\chi'_A(r) = 0$, for locating the A-enriched (i.e. the peaks on the line profiles in Fig. 3a)/A-depleted (i.e. the valleys on the line profiles in Fig. 3a) column positions; (ii) $\chi''_A(r) < 0$, for locating the A-enriched column positions (peaks on the line profiles); (iii) $\chi_A(r) > \bar{\chi}_A(r)$, where the $\chi_A(r)$ represents the concentration of A, and $\chi'_A(r)$, $\chi''_A(r)$, and $\bar{\chi}_A(r)$ are the 1st derivative, 2nd derivative, and average of A in the EDS line profiles, respectively. As an example, the 1st ($\chi'_{Cu}(r)$, dark grey solid line) and 2nd derivatives ($\chi''_{Cu}(r)$, light grey dotted line) related to M (M = Fe, Co, Ni, Cu, Al) for one of the EDS line profiles are plotted in Fig. 3a and Supplementary Fig. 8. The horizontal dotted lines indicate the average concentration of corresponding elements. The red, cyan, pink, orange, and green vertical lines indicate the locations of Cu-, Fe-, Co-, Ni-, and Al-enriched columns. After locating the explicit positions of the atomic columns, their spatial

distributions and correlation were systematically analyzed. The distance distributions between the A- and B-enriched columns were determined, where the A–B pair could be any two out of the Fe, Co, Ni, Cu, and Al. Fig. 3b and Supplementary Fig. 9 show the frequency distribution histograms of the distance between two atomic columns, where green, orange, and blue represent bin widths of 0.01, 0.015, and 0.02 nm, respectively.

To acquire more intuitive distribution regularities, two rectangles with different colors were plotted in the histograms (Fig. 3b and Supplementary Fig. 9), where the light red and blue rectangles were located at 0.19 ± 0.03 nm and 0.38 ± 0.03 nm, respectively. For the same atomic pairs, such as Fe-Fe, Co-Co, Ni-Ni, Cu-Cu, and Al-Al, the first peaks of frequency appeared at approximately 0.38 nm (light blue rectangles in Fig. 3b and Supplementary Fig. 9). The frequency at 0.19 nm (light red rectangles) was
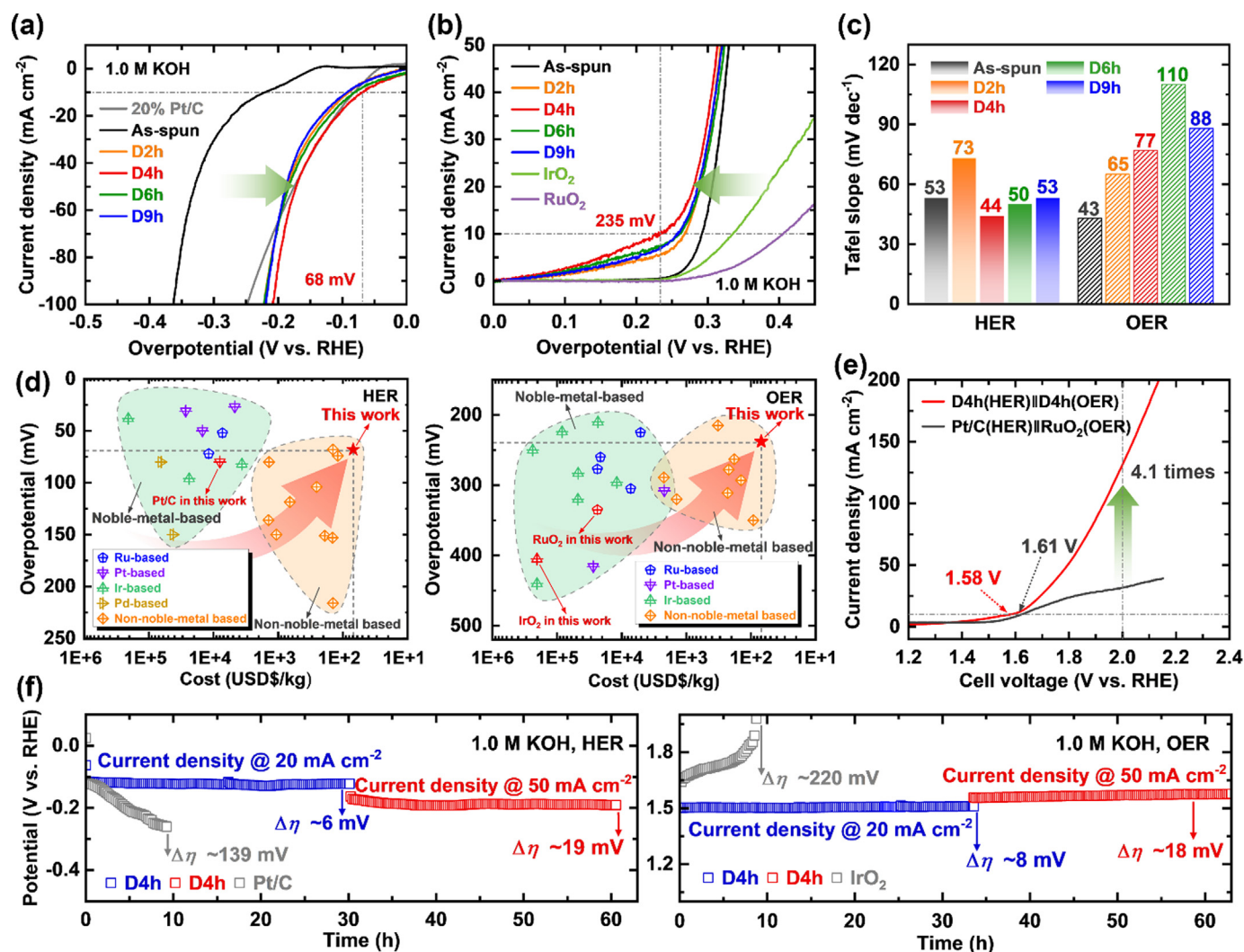
FIG. 4

Electrocatalytic performance of the MPEA for HER and OER in 1.0 M KOH solution. Polarization curves of (**a**) HER and (**b**) OER at a scan rate of 5 mV s^{-1} with *iR* loss correction. (**c**) Tafel slopes for HER and OER for the ribbons before and after dealloying. (**d**) Comparison of raw material costs of various HER and OER electrocatalysts and their overpotentials at the current density of 10 mA cm^{-2} in 1.0 M KOH. (**e**) Polarization curves of D4h‖D4h and Pt/C‖RuO$_2$ systems for overall water splitting with *iR* loss correction. (**f**) HER and OER stability performance of the D4h MPEA at current densities of 20 and 50 mA cm^{-2}, and the stability performance of the Pt/C (HER) and IrO$_2$ (OER) at a current density of 20 mA cm^{-2} without *iR* loss correction.

relatively low and approached zero, suggesting that the atomic columns enriched with the same element were separated by 2r^* (r^* is defined as the nearest-neighbor atomic distance, Fig. 3c). Thus, r^* was approximately 0.19 nm in this work. The mutual exclusion phenomenon of neighboring identical atoms has also been discovered in other MPEA systems [30,31,40], and such results were consistent with CSRO determined by the Monte Carlo simulation method [29,45]. With respect to the atomic columns enriched with unlike species, such as Al-Cu, Fe-Cu, Ni-Cu, and Co-Cu pairs, the frequencies at $r^* = 0.19$ nm were much higher, indicating that these atomic pairs were prone be first neighbor, consistent with the EDS mapping results presented in Fig. 2b–i. Moreover, the first-neighbor atomic distance measured from HRTEM was 0.23 nm (Fig. 2a), close to that obtained value from the statistical EDS line profiles ($r^* \approx 0.19$ nm). The higher frequency of the Al-Cu pair might be associated with the higher content of Al and Cu in BCC* phase (Supplementary Table 1).

The driving force for the formation of CSRO in the proposed MPEA might originate from the energy minimum principle, resulting from atomic spin polarization [29,39,40,45]. Notably, the components of our MPEA have different magnetic properties: Fe, Co, and Ni are ferromagnetic, Al is paramagnetic, and Cu is diamagnetic. Elemental pairs that are magnetically aligned with opposite-spin have a tendency to be preferred neighbors [39,45], which corresponds to the Fe-Cu, Co-Cu, Ni-Cu, and Al-Cu atomic pairs, whereas the same-spin pairs will be repulsive to achieve the energetically favorable states [29,39,40], which corresponds to the Fe-Fe, Co-Co, Ni-Ni, Cu-Cu, and Al-Al atomic pairs in this work.

Electrochemical analysis

The self-supported MPEA ribbons were directly used as working electrodes for investigating electrochemical water splitting performance in a 1.0 M KOH solution. Commercial Pt/C, IrO$_2$, and RuO$_2$ were used to perform a comparative analysis. The
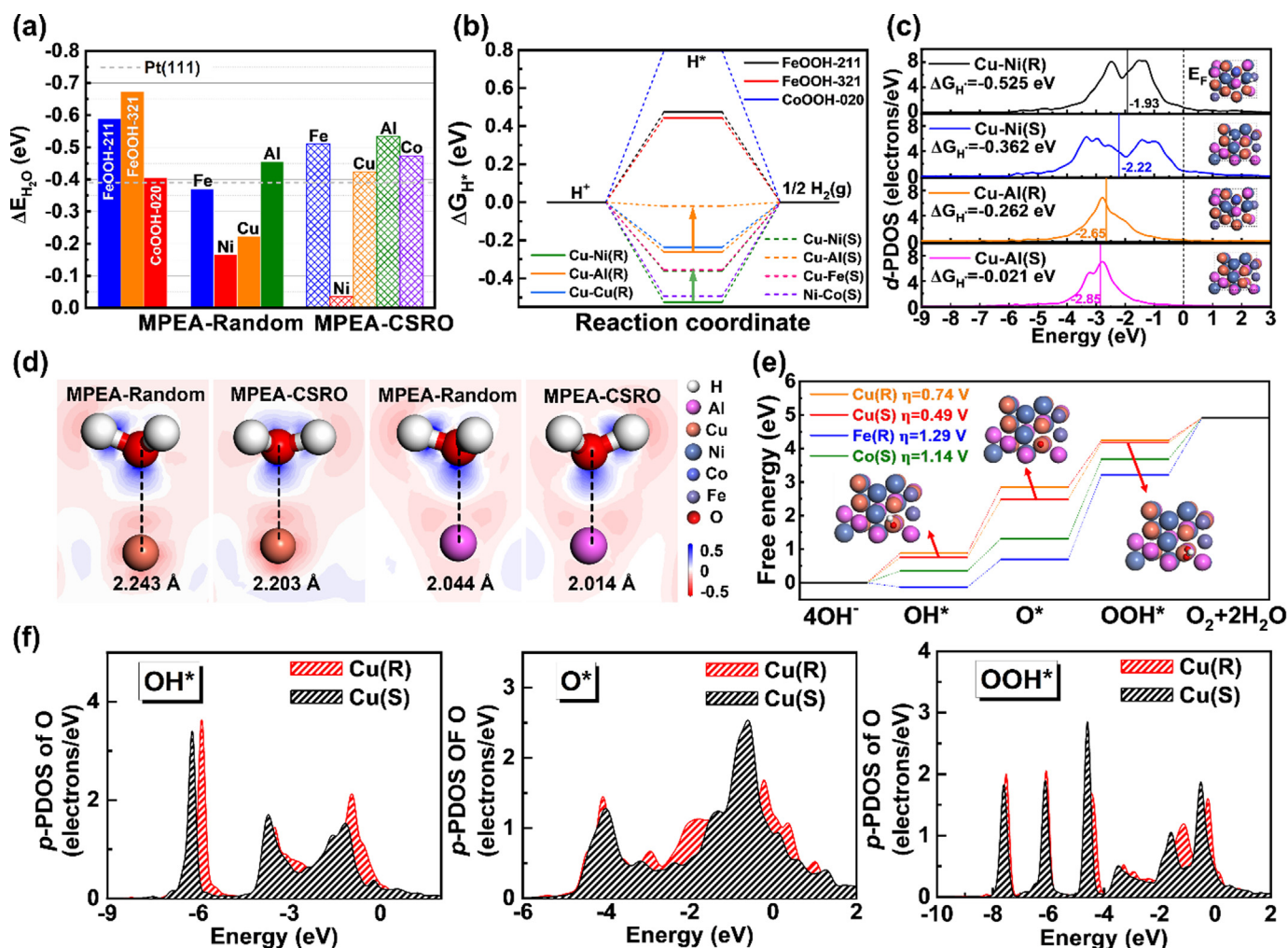
FIG. 5

DFT simulation results. (**a**) Calculated ΔE_{H_2O} for various sites in the FeOOH-211, FeOOH-321, CoOOH-020, MPEA-Random, and MPEA-CSRO models. As a reference, the ΔE_{H_2O} of Pt (111) surface is marked by the grey dashed line. (**b**) Gibbs free energy (ΔG_{H*}) profiles for various catalytic sites at the surfaces of the Pt (111), FeOOH-211, FeOOH-321, CoOOH-020, MPEA-Random, and MPEA-CSRO models. The arrows highlight the difference of ΔG_{H*} at the same elemental sites in the MPEA-Random and MPEA-CSRO models. '(R)' and '(S)' represent the active sites in MPEA-Random and MPEA-CSRO models, respectively. (**c**) The d-orbital partial density of states (d-PDOS) of the MPEA-Random and MPEA-CSRO models with H* adsorption onto Cu-Ni and Cu-Al bridge sites for each denoted as (R) and (S), respectively. The solid lines marked with energy values show the position of d-band centers and the dashed line indicates Fermi level (E_F). The insets show the corresponding atomic configurations after H* adsorption at the surface sites. (**d**) 2D electron density differences after H_2O adsorption onto Cu and Al sites in the MPEA-Random and MPEA-CSRO models. Red and blue represent the depletion and accumulation of electrons with the unit of $e/Å^3$, respectively. (**e**) Free energy profiles of Cu, Fe, and Co top sites in the MPEA-Random and MPEA-CSRO models at the zero potential ($U = 0$ V). η represents the overpotential. (**f**) p-orbital partial density of states (p-PDOS) of the O atom in OH*, O*, and OOH* species after their adsorption onto Cu sites in the MPEA-Random and MPEA-CSRO models denoted as (R) and (S), respectively.

potentials obtained in this work were iR-corrected to remove the ohmic drop across the electrolyte, unless specified otherwise. As shown in Fig. 4a and b, the D4h MPEA exhibited the lowest overpotentials of 68 mV and 235 mV for the HER and OER at a current density of 10 mA cm^{-2}, respectively, which were considerably lower than those of the as-spun MPEA ribbon (221 mV for HER and 292 mV for OER) and the commercial noble metal catalysts (Pt/C: 82 mV for HER; IrO$_2$: 335 mV for OER; RuO$_2$: 404 mV for OER). The Tafel slope of the D4h MPEA was 44 mV dec^{-1} for HER, which was the lowest value among the as-spun and dealloyed MPEAs (Fig. 4c), implying fast reaction kinetics based on the Volmer-Heyrovsky mechanism [50]. To

highlight the outstanding performance of the proposed MPEA, several state-of-the-art electrocatalysts for the HER and OER were selected for performance comparison (Supplementary Fig. 10, Supplementary Tables 4 and 5). The D4h MPEA with intrinsic CSRO and porous structure has lower overpotentials than other non-noble metal-based electrocatalysts, which approached those of the NiFe (oxy)hydroxides [51,52], noble-metal-based catalysts [53–55] and even the Ru single-atom catalysts [56,57]. To highlight the cost-effectiveness of our material, we compared the raw material costs of various electrocatalysts, including Pt-based, Ir-based, Pd-based, Ru-based, and non-noble-metal-based catalysts. As shown in Fig. 4d, Supplementary Tables 6 and 7,

our D4h MPEA ribbon presented favorable cost-effective trade-off relationship compared with other electrocatalysts. It exhibited close electrocatalytic performance compared to some of the noble-metal-based catalysts, while were several orders of magnitude cheaper than them and can be produced with a large-scale metallurgical technique. Considering the advantage of using relatively low-cost elements, our dealloyed MPEA ribbon presented great potential for practical application.

The ECSAs of the MPEA ribbons were evaluated via the C_{dl} obtained from CV curves at scanning rates of 10–50 mV s^{-1} (Supplementary Fig. 11). The D4h MPEA ribbon exhibited the largest ECSA (41 mF cm^{-2}) among the MPEA ribbons, which demonstrated its potential for enhancing the water splitting activity. EIS measurements were conducted to evaluate the electron transport ability of the MPEA ribbons. As shown in the Nyquist plots (Supplementary Fig. 12), the D4h MPEA ribbon displayed the smallest diameter of the characteristic semicircle, indicating improved electron transfer ability, which could enhance the electrocatalytic kinetics [58]. Considering the superior HER and OER performances, we used the D4h MPEA ribbons as both the cathode and anode for overall water splitting in a dual-electrode system (Fig. 4e). A cell voltage of 1.58 V was obtained at a current density of 10 mA cm^{-2}, which is lower than that of the Pt/C‖RuO$_2$ dual-electrode system (1.61 V). Supplementary Movie 1 presented the fast hydrogen and oxygen evolution when using a 1.5 V alkaline battery to drive the D4h‖D4h system to electrolyze water. Moreover, the current density of D4h MPEA (130 mA cm^{-2}) at the cell voltage of 2.0 V was about 4 times that of the noble-based Pt/C‖RuO$_2$ catalyst system (32 mA cm^{-2}). Supplementary Fig. 13 and Supplementary Table 8 present a comparison of the cell voltage of the proposed MPEA with recently reported electrocatalysts. The D4h MPEA exhibited a lower cell voltage than those of the reported non-noble-based electrocatalysts.

Chronoamperometry tests were employed to evaluate the stability of the D4h MPEA ribbon. Commercial Pt/C and IrO$_2$ were also employed for comparison. As shown in Fig. 4f for the HER stability test, only slight declines of 6 and 19 mV were found after testing for 60 h at current densities of 20 and 50 mA cm^{-2}, respectively. In contrast, the performance of the commercial Pt/C catalyst deteriorated 139 mV after less than 10 h at current density of 20 mA cm^{-2}. For the OER stability test, the increase of the overpotential of the D4h MPEA ribbon (8 and 18 mV at the current densities of 20 and 50 mA cm^{-2}, respectively) was much lower than that of the IrO$_2$ electrode (220 mV, at a current density of 20 mA cm^{-2}). Moreover, the self-supported and porous structure of MPEA ribbon was strong and stable enough to bear the large shear stress caused by fast H$_2$ and O$_2$ bubble evolution, which is one of the main reasons leading to the peeling of powder electrocatalysts from substrates and thus the degradation of performance [59,60]. The structural and compositional stability of the D4h MPEA were also investigated after the durability tests. ICP-OES results show that negligible concentrations of Fe, Co, Ni, Cu, and Al elements were dissolved into electrolyte after the durability tests (Supplementary Table 9). Moreover, the porous surface morphology and dual-phase structure of the used D4h ribbon were still well maintained after stability testing (Supplementary Fig. 14). The corresponding SAED pattern of the

BCC⋆ phase still exhibited CSRO characteristic (Supplementary Fig. 15, white arrows), although the SAED pattern of the NC phase presented some degree of amorphization. For the BCC⋆ phase, the d-spacings of the $\{0\,1\,\bar{1}\}$ and $\{\bar{1}\,0\,1\}$ planes were measured to be 0.202 and 0.203 nm, respectively. Additionally, the d-spacings of 0.204, 0.197, 0.254, and 0.214 nm were indexed specifically to the {321}, {411}, {211} planes for FeOOH and the {200} plane for CoOOH (Supplementary Figs. 16 and 17). These values were found to be consistent with those measured prior to the durability tests (Fig. 1c). In terms of the elemental distributions of the used D4h MPEA ribbon, Fe, Co, and O were still highly concentrated in the NC phase, while the Fe, Co, Ni, Cu, and Al were still enriched in the BCC⋆ phase (Supplementary Fig. 14 and Supplementary Table 1). The XPS profiles of the used MPEA ribbon indicated that the zero-valent metallic elements transformed to higher valence states (Supplementary Fig. 18), revealing the contribution of chemical synergetic effect to the excellent electrocatalytic performance.

Benefits of CSRO on HER and OER

According to the experimental characterization results, the (oxy)hydroxides in the NC phase and the CSRO structure of the BCC⋆ phase may play important roles in the excellent overall water splitting performance. To elucidate the exact atomistic mechanisms, a series of atomistic models including FeOOH-211, FeOOH-321, CoOOH-020, and MPEA phases without and with CSRO (denoted as MPEA-Random and MPEA-CSRO, respectively) were established and used in DFT calculations to investigate the contributions of the NC and BCC⋆ phases to the overall water splitting ability. The ΔE_{H_2O} at various sites on the catalyst surface were calculated, as shown in Fig. 5a. The results indicated that the FeOOH phase contributes to H$_2$O adsorption, with the ΔE_{H_2O} values of FeOOH-211 and FeOOH-321 being −0.59 and −0.67 eV, respectively. Moreover, the ΔE_{H_2O} at Fe, Co, Cu, and Al sites in MPEA-CSRO were greatly improved compared to those at the sites in the MPEA-Random model, presenting better H$_2$O adsorption ability than that of Pt (111) sites. The improved ΔE_{H_2O} at Fe, Cu and Al sites in the MPEA-CSRO model are attributed to their stronger interaction than the same-element sites in MPEA-Random counterparts, resulting in shortened bonding distances (Supplementary Table 10). Partial density of states (PDOS) was analyzed to further explore the binding strength between H$_2$O and the active sites. As shown in Supplementary Fig. 19a, the adsorbed O atom in H$_2$O exhibited an affinity for the Fe sites in FeOOH-211 model, with the hybridization energies centered at −9.7, −6.5, and −4.7 eV, respectively. Significant left shifts of the interaction positions (−10.5, −7.6, and −5.6 eV) far from the Fermi level were observed in the FeOOH-321 model, indicating improved adsorption strength between the Fe site and O atom in H$_2$O [61,62]. Encouragingly, strong left shifts of the interaction positions far from the Fermi level were also demonstrated for the Fe and Al sites in the MPEA-CSRO model, (Supplementary Fig. 19b and d). However, strong right shifts of the interaction positions close to the Fermi level were observed for the Ni sites in the MPEA-CSRO model (Supplementary Fig. 19c), resulting in lower adsorption affinity for the H$_2$O molecules. The enhanced H$_2$O adsorption capacity of Cu sites in

MPEA-CSRO model could not be well explained by the shifts in the interaction positions (Supplementary Fig. 19e). As shown in Fig. 5d, the local 2D electron density difference after H_2O adsorption onto the Cu and Al sites were compared to probe the effect of CSRO on the charge transferability of Cu and Al sites to the O atom in H_2O. The charge transferability of the Cu sites in the MPEA-CSRO model was stronger than that in the MPEA-Random model, with a shortening of the bond distance. These results show that the formation of oxyhydroxides and CSRO structure effectively facilitate the H_2O adsorption capacity.

With respect to the HER activity, the ΔG_{H*} was analyzed at various active sites on the surface of the established models. A series of atomic configurations with stable H* adsorption and the corresponding ΔG_{H*} are presented in Supplementary Fig. 20. It is well accepted that the HER process including reversible adsorption and desorption of H* requires that the interaction between catalytic sites and H* is neither too strong nor too weak [63]. It was found that both Fe and Co sites in the oxyhydroxides exhibited large ΔG_{H*} values due to their too weak interaction with H* (Fig. 5b), which is consistent with the d-band center shift results (Supplementary Fig. 21). For the MPEA models, it was demonstrated that the main active sites were bridge sites, and most of them presented better ΔG_{H*} than the active sites in oxyhydroxides. As shown in Fig. 5b, the ΔG_{H*} values of the Cu-Ni and Cu-Al sites in the MPEA-CSRO models were greatly improved relative to the MPEA-Random models and approached zero. In particular, the ΔG_{H*} value of the Cu-Al site was as small as -0.021 eV (Supplementary Table 11), which is even lower than that of the Pt (111) site (-0.107 eV), demonstrating that the Cu-Al sites in the CSRO region provide a significant contribution to enhance the HER activity. Moreover, the d-band centers of the Cu-Ni and Cu-Al bridge sites in the MPEA-CSRO model shift farther from Fermi level than is seen in the MPEA-Random model (Fig. 5c), indicating that the formation of CSRO regions effectively mitigate the too strong interaction between H* and Cu-Ni and Cu-Al sites, thus improving the HER performance.

The atomistic mechanisms of promoting OER activity were also explored by DFT calculations. The free energy profiles of the OER process at various sites in our models are shown in Fig. 5e, Supplementary Fig. 22, and Supplementary Table 12. The rate-determining step (RDS) of the OER process for all active sites in the oxyhydroxides and MPEA models was the transition from O* to OOH* ($\Delta G_3 = \Delta G_{OOH*} - \Delta G_{O*}$) except for the Cu sites, the RDS for which was the transition from OH* to O* ($\Delta G_2 = \Delta G_{O*} - \Delta G_{OH*}$). First, The Co sites in the CoOOH-020 model exhibited superior OER performance to that of the Fe sites in FeOOH-211 and FeOOH-321 models owing to the weaker interaction between O* and Co sites, with a relatively low overpotential of $\eta = 0.83$ V (Supplementary Fig. 22a). The CSRO slightly improved the overpotential for the Cu-Ni and Cu-Al bridge sites in the MPEA models, though they were still unfavorable for efficient OER performance, which is attributed to the strong interaction between O* and bridge sites (Supplementary Fig. 22b). Surprisingly, the Cu top sites in the MPEA-CSRO models exhibited considerably lower overpotentials of $\eta_{Cu(R)} = 0.74$ V

and $\eta_{Cu(S)} = 0.49$ V than the other active sites (Fig. 5e), indicating the significant role of CSRO in our MPEA. Furthermore, the Cu sites in the MPEA-CSRO model effectively avoid the too weak binding energy between the Cu sites and O*, and thus further enhancing the ΔG_2 for efficient OER performance. The atomic configurations of the reaction steps for the Co sites in the CoOOH-020 models and the Cu sites in the MPEA-Random and MPEA-CSRO models are shown in Supplementary Figs. 23 and 24, respectively. The left shift of the O atom p-orbitals for the Cu sites in MPEA-CSRO model (black shadow in Fig. 5f) indicates enhanced interaction of OH* and OOH* with the Cu sites relative to the MPEA-Random model (red shadow in Fig. 5f). Furthermore, by comparison of the 2D electron density difference of O* and Cu sites in the MPEA-Random and MPEA-CSRO models (Supplementary Fig. 25) highlighted that the interaction intensity between the O* and Cu sites was greatly enhanced by the CSRO, and thus improve the corresponding overpotential.

Discussions

In this work, chemical short-range order was demonstrated to enhance the electrochemical water splitting performance of a multi-principal element alloy. Furthermore, we have developed a low-cost and freestanding dual-phase $Fe_{10}Co_5Ni_{10}Cu_{15}Al_{60}$ MPEA ribbon exhibiting CSRO preferential atomic pairs of M-Cu (M = Fe, Co, Ni, Al) in the BCC phase along with Fe/CoOOH metal oxyhydroxide phases that combine to provide the excellent electrocatalytic behavior in alkaline condition. The MPEA ribbons can be directly employed as bifunctional electrodes for overall water splitting and they presented ∼4 times performance that of the noble Pt/C||RuO₂ dual-electrode system and it exhibited negligible performance degradation and structural deterioration over 60 h. This performance was attributed to the CSRO structure enhancing the H_2O adsorption ability, optimizing the electronic structure to stabilize adsorption/desorption of hydrogen protons for the hydrogen evolution reaction, as well as reducing the energy barrier of the rate-determining step for the oxygen evolution reaction, thus synergistically contributing to the overall water splitting. Our study reveals a beneficial role of chemical short-range order and the resulting chemical heterogeneities behind the electrocatalytic activity in multi-principal element alloys, thus providing a novel alloy design strategy for the future development of compositionally complex alloys for widespread electrocatalytic applications.

CRediT authorship contribution statement

Xinyue Zhang: Data curation, Methodology. **Yongjie Li:** Formal analysis. **Liliang Shao:** Data curation, Formal analysis, Funding acquisition, Supervision, Writing – review & editing. **Siyi Di:** Formal analysis. **Juan Kuang:** Supervision, Writing – review & editing. **Lai-Chang Zhang:** Formal analysis, Writing – review & editing. **Jamie J. Kruzic:** Writing – review & editing. **Yang Lu:** Formal analysis, Funding acquisition, Supervision, Validation, Writing – review & editing. **Jian Lu:** Supervision, Writing – review & editing. **Baolong Shen:** Formal analysis, Funding acquisition, Supervision, Validation, Writing – review & editing.

Data availability

Data will be made available on request.

Declaration of competing interest

The authors declare that they have no known competing financial interests or personal relationships that could have appeared to influence the work reported in this paper.

Acknowledgments

Author contributions

Conceptualization: Z. J., L.G.S., Y. Lu., and B.L.S., Methodology: Y.Y.Y., X.Y.Z., Y.J.L., Q.Q.W., Y.J.L., L.L.S., S.Y.D., and J.K., Investigation: Y.Y.Y., Z. J., X.Y.Z., L.G.S., and Y.J.L., Visualization: Y.Y.Y., Z. J., L.G.S., Y.J.L., Funding acquisition: Z.J., L.G.S., Y. Lu., and B.L.S., Project administration: Z.J., L.G.S., and B.L.S., Supervision: Z.J., L.G.S., Y. Lu., and B.L.S., Writing – original draft: Y.Y.Y., Z.J., and L.G.S., Writing – review & editing: Y.Y.Y., Z.J., L.G.S., Q.Q.W., L.C.Z., J.J.K., Y. Lu., J.L., and B.L.S.

Data and materials availability

All data are available in the main text or the supplementary materials.

Appendix A. Supplementary material

Supplementary material to this article can be found online at https://doi.org/10.1016/j.mattod.2023.12.006.

References

[1] G. Glenk, S. Reichelstein, Nat. Energy 4 (3) (2019) 216–222.
[2] M.-S. Balogun et al., Mater. Today 20 (8) (2017) 425–451.
[3] X. Wang et al., Mater. Today 36 (2020) 125–138.
[4] J. Song et al., Chem. Soc. Rev. 49 (7) (2020) 2196–2214.
[5] X. Kang et al., Nat. Commun. 14 (1) (2023) 3607.
[6] X. Ren et al., Nat. Commun. 14 (1) (2023) 2482.
[7] J.-W. Yeh et al., Adv. Eng. Mater. 6 (2004) 299–303.
[8] Y. Yao et al., Science 376 (6589) (2022) eabn3103.
[9] B. Jiang et al., Science 371 (2021) 830–834.
[10] Y. Zhang et al., Prog. Mater. Sci. 61 (2014) 1–93.
[11] E.P. George et al., Nat. Rev. Mater. 4 (8) (2019) 515–534.
[12] Y.-H. Liu et al., Sci. Adv. 9 (2023) eadf9931.
[13] N. Zhang et al., Nat. Commun. 11 (1) (2020) 4066.
[14] V. Chaudhary et al., Mater. Today 49 (2021) 231–252.
[15] Z. Wang et al., Mater. Today 54 (2022) 83–89.
[16] X. Feng et al., Mater. Today 42 (2021) 10–16.
[17] M. Cui et al., Sci. Adv. 8 (2022) eabm4322.
[18] Z. Jia et al., Adv. Mater. 32 (21) (2020) 2000385.
[19] M.W. Glasscott et al., Nat. Commun. 10 (1) (2019) 2650.
[20] Z. Jia et al., Adv. Funct. Mater. 31 (38) (2021) 2101586.
[21] X. Zhang et al., Adv. Mater. 35 (38) (2023) 2303439.
[22] L.-C. Zhang et al., Prog. Mater. Sci. 105 (2019) 100576.
[23] A. Sarkar et al., Adv. Mater. 31 (26) (2019) 1806236.
[24] T. Li et al., Nat. Catal. 4 (1) (2021) 62–70.
[25] C. Oses et al., Nat. Rev. Mater. 5 (4) (2020) 295–309.
[26] M.Q. Wang et al., Angew. Chem. Int. Ed. 57 (7) (2018) 1963–1967.
[27] M. Cui et al., Adv. Energy Mater. 11 (3) (2020) 2002887.
[28] X. Zhao et al., J. Mater. Chem. A 7 (46) (2019) 26238–26242.
[29] J. Ding et al., Proc. Natl. Acad. Sci. 115 (36) (2018) 8919–8924.
[30] X. Chen et al., Nature 592 (7856) (2021) 712–716.
[31] L. Zhou et al., Acta Mater. 224 (2022) 117490.
[32] Z. Lei et al., Nature 563 (7732) (2018) 546–550.
[33] Y. Bu et al., Mater. Today 46 (2021) 28–34.
[34] S. Chen et al., Mater. Today 65 (2023) 14–25.
[35] A. Fantin et al., Acta Mater. 193 (2020) 329–337.
[36] Q. Ding et al., Nature 574 (7777) (2019) 223–227.
[37] A. Fernández-Caballero et al., J. Phase Equilibria Diffus. 38 (4) (2017) 391–403.
[38] Y. Wu et al., J. Mater. Sci. Technol. 62 (2021) 214–220.
[39] F. Walsh et al., Proc. Natl. Acad. Sci. 118 (13) (2021) e2020540118.
[40] R. Zhang et al., Nature 581 (7808) (2020) 283–287.
[41] Z. Su et al., Acta Mater. 245 (2023) 118662.
[42] D.J. Chadi, Phys. Rev. B 16 (4) (1977) 1746–1747.
[43] J.K. Nørskov et al., J. Electrochem. Soc. 152 (2005) J23–J26.
[44] X.L. Wang et al., Angew. Chem. Int. Ed. 57 (31) (2018) 9660–9664.
[45] A. Tamm et al., Acta Mater. 99 (2015) 307–312.
[46] Z. Jia et al., ACS Mater. Lett. 4 (8) (2022) 1389–1396.
[47] X. Gao et al., Acta Mater. 141 (2017) 59–66.
[48] L. Zhang et al., Mater. Lett. 216 (2018) 252–255.
[49] Z. Cai et al., Adv. Energy Mater. 12 (21) (2022) 2103923.
[50] X. Zhang et al., Chem. Eng. J. 426 (2021) 131524.
[51] F. Dionigi et al., Nat. Commun. 11 (1) (2020) 2522.
[52] Z. He et al., Nat. Commun. 13 (1) (2022) 2191.
[53] G. Chen et al., Adv. Mater. 30 (10) (2018) 1706279.
[54] M. Liu et al., Adv. Mater. Interfaces 6 (7) (2019) 1900015.
[55] Z. Liu et al., J. Mater. Chem. A 7 (10) (2019) 5621–5625.
[56] Y. Hu et al., Adv. Energy Mater. 11 (1) (2020) 2002816.
[57] Z. Yu et al., Appl. Catal. B 310 (2022) 121318.
[58] Y.P. Wu et al., Angew. Chem. Inter. Ed. 56 (42) (2017) 13001–13005.
[59] X. Zhang et al., Small 15 (42) (2019) e1903297.
[60] Q. Yu et al., Nat. Commun. 12 (1) (2021) 6051.
[61] Z. Chen et al., Nat. Commun. 13 (1) (2022) 763.
[62] C. Wei et al., Adv. Mater. 31 (31) (2019) 1806296.
[63] J. Greeley et al., Nat. Mater. 5 (11) (2006) 909–913.